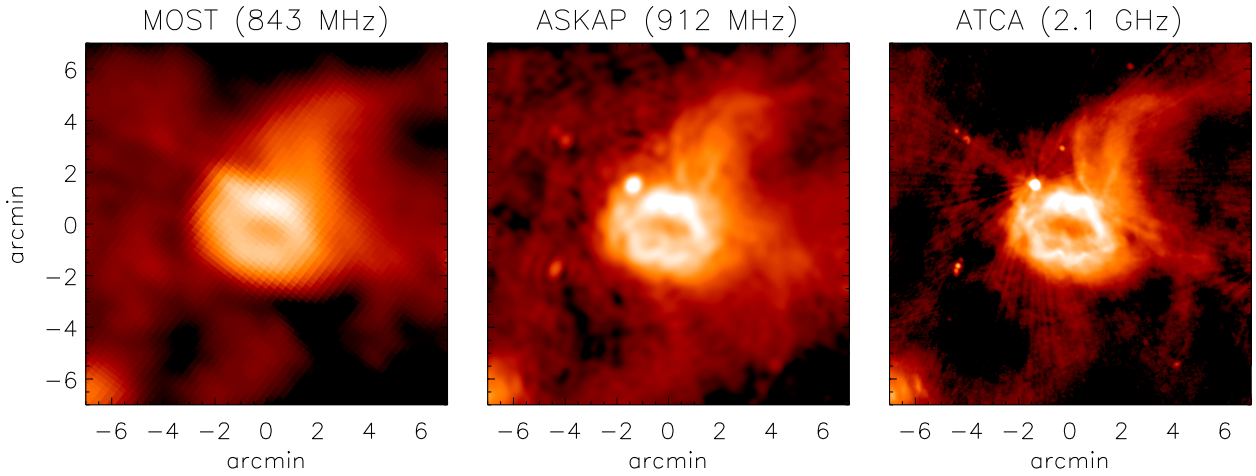

Figure 5. Images of the H II region [C06] S17 as observed with MOST, ASKAP, and ATCA.

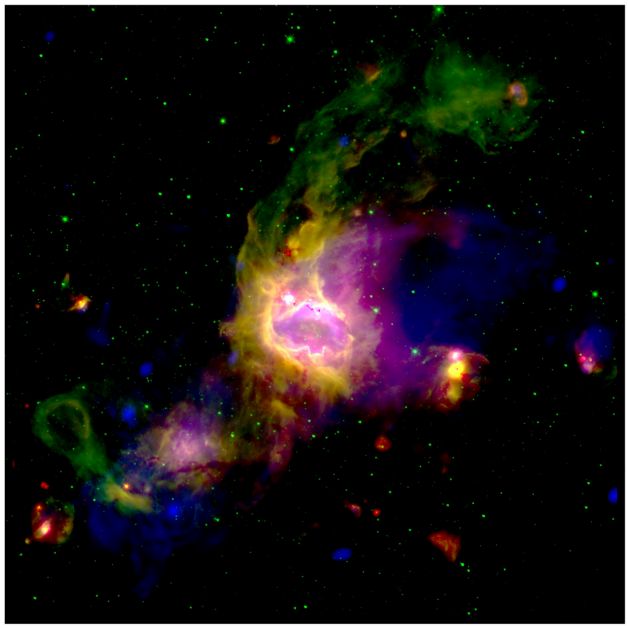

Figure 6. An RGB false colour image of the field around S17 in both dust and ionized gas. The colour-code is: green, from Spitzer/Glimpse (IRAC, 8 μm); red, from Herschel/Hi-GAL (PACS, 70 μm); and blue, from the ASKAP, 912 MHz. The image, 33 arcmin × 33 arcmin in size, is centred at l,b = 343.48°, 0.026°. The position of the S17 Bubble, as reported in Churchwell et al. (2006), is l,b = 343.482°, −0.044°.

In the following analysis, the detection of known radio H II regions, PNe, and SNRs by our ASKAP observation are assessed by visual inspection at positions provided by relevant catalogues.

As the purpose of this paper is a summary of the project focusing on the potentiality of the ASKAP in the field of Galactic radio astronomy, for each different category of Galactic sources considered in this section, we will exclusively provide the source identification and, if present in the compact catalogue provided by SELAVY, the integrated flux density. As indicated in session 3.1, a source is extracted by SELAVY if it satisfies the detection criterion (flux density $\geq 5\sigma$, where σ is the local rms), and if its spatial structure can be accurately fitted by a small number of Gaussian components (Whiting & Humphrey 2012).

3.3.1 H II regions

H II regions are found in star-forming sites, in the vicinity of high-mass stars, where the gas is ionized by ultraviolet photons from the central object. They are tracers of the current epoch star formation and their continuum radio emission is due to thermal Bremsstrahlung radiation. The most complete catalogue of Galactic H II regions has been compiled by Anderson et al. (2014). To select H II regions, the authors used mid-infrared (MIR) observations from the Wide-Field Infrared Survey Explorer (WISE) satellite, taking advantage of the typical morphology that H II regions show in the MIR. The Anderson et al. (2014) catalogue has 8399 entries and consists of 1524 sources with robust classification as true H II regions, because they have measured RRL or H_α emission. The others are classified as *candidates*, either with spatially coincident radio continuum emission (1986 sources) or without a radio counterpart (4124 sources). The latter are indicated in the catalogue as *radio quiet*. Among the possible *candidates*, there are 115 with no radio data available.

Within the ASKAP SCORPIO region, there are 382 sources, catalogued by Anderson et al. (2014) as follows: 97 known H II regions (K), 38 candidates (C), 220 radio quiet (Q), 22 closely located to a known H II regions (G), and five without radio data available. From a visual inspection of the ASKAP SCORPIO field we conclude that all 97 known (K), all 38 candidate (C) and all 22 grouped (G) H II regions were detected. Furthermore, 99/220 of radio-quiet sources (Q) and all of the five sources, which were previously reported without radio data available, were also detected in our ASKAP observations, bringing the total number of detections to 261. Fig. 7 shows a portion of the ASKAP SCORPIO field with the H II regions from Anderson et al. (2014) highlighted.

Ingallinera et al. (2019) present a catalogue of extended sources detected with ATCA in the SCORPIO sub-field. They extracted 99 extended sources, including nine H II regions reported by Anderson et al. (2014) as radio quiet and pointed out the presence of 18 H II regions, previously indicated as radio quiet, detected as point sources, without providing, however, their name or positions. Eight out of the nine extended sources, reported by Ingallinera et al. (2019), are also

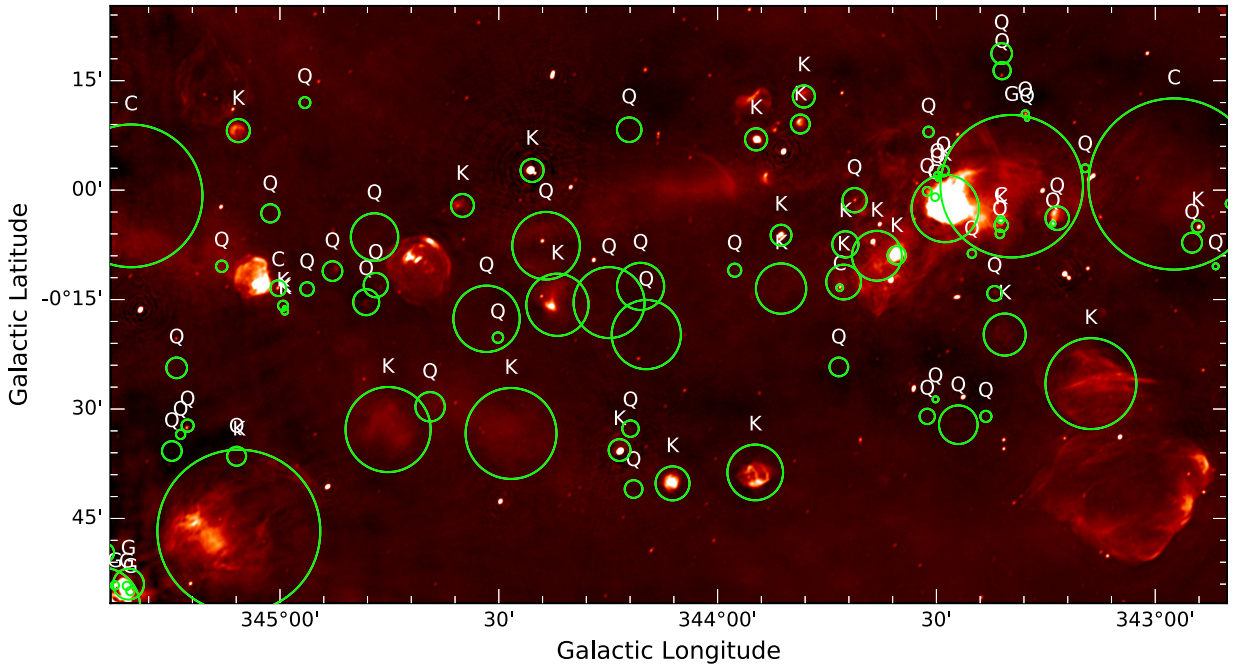

Figure 7. A portion of SCORPIO field centred at position l,b = 343.8°, −0.2°. The H II regions defined by Anderson et al. (2014) are indicated as 'C' *candidates*, 'K' *known*, 'G' *group*, 'Q' *quiet*.

present in our sample of sources detected by visual inspection of our ASKAP image, but we were not able to check if any other sources were in common. Our final sample of new detections consists of the 5/5 with no radio observations available plus the 91 previously reported as radio quiet, yielding a total of 96 new detections.

As anticipated in Section 3.3, we produce a catalogue for the 112 sources detected by visual inspection and extracted by SELAVY (Table 2). The catalogue reports the object WISE name as in Anderson et al. (2014), the coordinates (RA and Dec.), the classification following Anderson et al. (2014), the integrated flux density and its associated error, the angular dimensions of the source, FWHM of the major ($\theta^d_{\rm max}$) and the minor ($\theta^d_{\rm min}$) axes of the source, as determined by the Gaussian fit, deconvolved by the synthesized beam. Table 2 is truncated and its complete version is available in the online version of the paper.

In the ASKAP image we detect 45 per cent of the sources previously classified as radio quiet. Anderson et al. (2014) provide different hypotheses on the nature of these radio-quiet H II regions candidates. Among them, the possibility that these sources, characterized in the MIR by the same morphology as H II regions, could be instead intermediate-mass stars that do not have the necessary UV radiation to ionize the nebula surrounding the central object, or perhaps H II regions in the very early or very late stage of their evolution. These authors, however, provide a hint on the angular dimension of the infrared selected radio-quiet H II regions. When considering the angular size distribution for WISE catalogue of H II regions, all the known, candidates, and group samples share the same distribution while the radio-quiet sources are significantly smaller. Since there is a relation between the dimension of the infrared and of the radio nebula (Bihr et al. 2016), we should expect to see different angular size distributions for the known H II regions and radio-quiet sources detected in our ASKAP image. In Fig. 8, the flux density and the angular dimension distributions for known (K) and radio-quiet (Q) H II regions, detected and extracted by SELAVY, are shown. The angular size plotted in Fig. 8 is defined as $\theta = \sqrt{(\theta^d_{\rm max})^2 + (\theta^d_{\rm min})^2}$.

In general, radio-quiet H II regions appear to be fainter and more compact than known (K) H II regions and this corroborates the hypothesis that previous non-detections were related to sensitivity limits of previous radio surveys. Similar result has been very recently obtained by Armentrout et al. (2021), who performed sensitive 3 cm JVLA observations targeting a sample of infrared-identified 'radio-quiet' H II regions in the range $245° \geq l \geq 90°$.

Since no information on distance of our detected sample of sources previously classified as radio quiet is available, we are not able to reach a conclusion on their physical dimension. These H II regions candidates are either close and compact, if they are in the early stage of their evolution or more distant if more evolved.

The detection of several sources previously classified as radio quiet indicates the high potential of ASKAP observations for Galactic studies as a significant number of radio-quiet H II regions candidates are possibly H II regions detected via their radio continuum near 1 GHz. The ASKAP performance will improve even further when the full 36 antenna array data will be used, allowing for more sensitivity and higher angular resolution. Further investigations, using a wider sample of candidate radio-quiet H II regions detected with the ASKAP in its final configuration, will allow us to further constrain the nature of these sources.

3.3.2 *Planetary nebulae*

Thermal radio continuum is also radiated by the ionized nebulae known as Planetary Nebulae (PNe). The PN is a short-lived (a few 10^4 yr) evolutionary phase of stars with mass between 0.8 and 8 $M_\odot$. Objects in this phase are of high relevance in recycling matter in the universe. They are responsible for enriching galaxies with

Table 2. H II regions and H II regions candidates detected and extracted with SELAVY. This truncated table is intended to show its content. The complete table is available in the online version of the journal.

SourceID	Obj. name [ABB2014] WISE	RA	Dec.	C	S_{912} (mJy)	err (mJy)	$\theta^d_{\rm max}$ (arcsec)	$\theta^d_{\rm min}$ (arcsec)
J252.386-44.4413	G340.910+00.167	16:49:32.5	−44:26:28	K	407.62	4.17	170.6	165.6
J252.609-44.2916	G341.121+00.141	16:50:26.1	−44:17:29	Q	5.73	0.09	39.4	25.1
J253.083-44.4688	G341.207−00.232	16:52:20.0	−44:28:07	K	710.53	17.04	51.7	42.6
J252.505-44.0838	G341.238+00.335	16:50:01.1	−44:05:01	K	9.62	0.11	30.9	19.8
J253.177-44.4449	G341.271−00.265	16:52:42.4	−44:26:41	Q	35.74	0.25	29.1	20.9
J252.734-44.1584	G341.286+00.159	16:50:56.2	−44:09:30	Q	2.13	0.02	18.1	0
J252.726-44.1177	G341.314+00.190	16:50:54.3	−44:07:03	Q	20.84	0.11	12.6	4.8
J253.277-44.3868	G341.358−00.287	16:53:06.5	−44:23:12	K	82.14	1.29	76.5	65.6
J252.806-44.1087	G341.364+00.147	16:51:13.4	−44:06:31	Q	4.96	0.24	54.5	13.8
J252.637-43.9016	G341.438+00.383	16:50:32.8	−43:54:05	C	2.55	0.05	27.5	11.4
–								

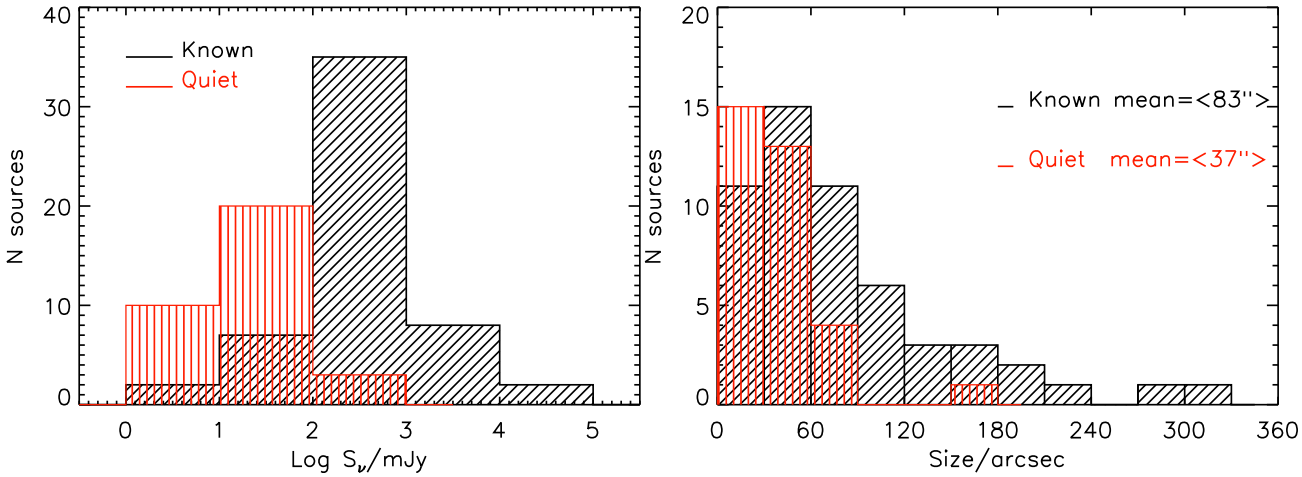

Figure 8. Flux density distribution (left-hand panel) and angular size distribution (right-hand panel) of H II regions, known, and radio quiet, detected with the ASKAP and extracted with SELAVY (see Table 2).

elements produced by stellar nucleosynthesis and thus trace the Galactic chemical enrichment process (Kwok 2007).

Parker et al. (2016) have compiled the most recent catalogue of Galactic Planetary Nebulae (HASH: Hong Kong/ AAO/ Strasbourg/ Hα). This catalogue is a unique data repository with a graphical interface, and currently contains multiwavelength images, spectra, positions, sizes, and morphologies of 3540 objects. For the following analysis we used the version as of 2016. These objects are classified as 2401 true (T) Galactic PNe, based on their multiwavelength PN-type morphologies and spectral features, 447 likely (L) Galactic PNe, based on the same parameters as for true PNe but with not completely conclusive imagery or spectroscopy, and 692 probable (P) Galactic PNe, where the available spectroscopy and/or imagery is not conclusive because of very low S/N spectra or a very low surface brightness of the nebula.

Within the ASKAP SCORPIO region, there are 48 sources catalogued by Parker et al. (2016), comprising 35 T, 6 L, and 7 P Galactic PNe. In the ASKAP map we detect 29/35 true PNe, 3/6 likely PNe, and 2/7 probable PNe, for a total of 34 radio sources.

In the case of true PNe, only 14 out of the 29 detected in the ASKAP maps have been already detected in the radio (Parker et al. 2016). We have therefore doubled the radio detections for these robustly classified Galactic PNe. We have further inspected the field of the non-detected true PNe. Four out of six of them are located in a region with strong confusion, while the fifth is located in a region with a local rms of about 200 μJy. The last one is very weak and barely distinguishable from the noise.

It is also worthwhile to underline our new detections of three likely and two probable Galactic PNe that, considering the 15 new detections among our sample of true PNe, brings the total number of new detections to 20.

All the results are summarized in Table 3, where the object name, in bold if it is a new detection, the coordinates (RA and Dec.), the Galactic coordinates, the classification as in Parker et al. (2016), the integrated flux and its associated error, as determined with SELAVY, are reported. Four sources, detected by visual inspection, were not extracted by SELAVY. This failure of the source finder algorithm is probably related to a highly noisy background around these sources or to the fact that these sources do not fulfil all the imposed criteria. Fig. 9 shows these sources, while all the (other) new detections are shown in Fig. 10.

3.3.3 Supernova remnants

Other major polluters of the Galaxy are SNRs, the remains following the explosion of their progenitor stars. By enriching the interstellar medium (ISM) in heavy elements and other nucleosynthesis products, these stellar ejecta contribute to the chemical composition of

Table 3. PNe detected in the ASKAP SCORPIO field. New detections are highlighted in bold. Sources for which no flux density is reported are only detected by visual inspection. Column C indicates the classification following Parker et al. (2016).

Obj. name	RA	Dec.	l	b	C	S_{912} (mJy)	err (mJy)
PHR J1642−4212	16:42:18.6	−42:14:45.20	341.723	+2.597	T	6.91	0.05
PN SuWt 3	16:44:24.1	−40:03:20.4	343.639	+3.733	T	3.68	0.04
Vd 1-3	16:49:32.9	−39:21:08.96	344.818	+3.432	T	2.48	0.04
MPA J1650−4030	16:50:20.2	−40:30:03.17	344.030	+2.582	T	5.5	0.05
Vd 1-4	16:50:25.3	−39:08:18.89	345.091	+3.439	T	3.23	0.03
Vd 1-5	16:51:33.7	−40:02:55.64	344.528	+2.690	T	4.99	0.06
PN H 1-3	16:53:31.3	−42:39:22.39	342.744	+0.752	T	35.18	0.14
PHR J1653−4143	16:53:55.3	−41:43:59.81	343.507	+1.277	T	14.59	0.07
Vd 1-6	16:54:27.3	−38:44:10.39	345.900	+3.086	T	14.35	0.13
MPA J1654−4041	16:54:43.2	−40:41:46.64	344.407	+1.814	L	9.53	0.06
PN G343.6+01.1	16:54:51.0	−41:43:49.91	343.618	+1.145	P	7.18	0.18
IRAS 16515−4050	16:55:00.4	−40:55:34.64	344.262	+1.627	T	8.72	0.03
PN G345.8+02.7	16:55:51.9	−39:00:20.95	345.862	+2.704	T		
PM 1-119	16:56:34.0	−43:46:14.77	342.226	−0.380	T	107.05	0.36
MPA J1656−3912	16:56:40.1	−39:12:36.83	345.800	+2.454	T	3.75	0.03
PN H 1-5	16:57:23.7	−41:37:57.86	343.992	+0.835	T		
IC 4637	17:05:10.5	−40:53:08.45	345.479	+0.140	T	233.11	0.62
Vd 1-9	17:05:38.9	−43:56:20.36	343.100	−1.775	T	9.54	0.10
PN Pe 1-8	17:06:22.6	−44:13:09.95	342.955	−2.049	T	83.62	0.39
Kn 98	17:06:19.6	−43:15:33.00	343.716	−1.463	L	7.19	0.07
MPA J1706−4434	17:06:49.3	−44:34:34.64	342.717	−2.327	T	8.32	0.07
PN H 1-6	17:06:59.1	−42:41:09.13	344.247	−1.215	T	34.85	0.12
Wray 16 251	17:07:30.6	−44:22:50.27	342.948	−2.308	T	37.89	0.29
PN G343.9−01.6	17:07:57.0	−43:09:04.93	343.980	−1.635	T	6.22	0.09
PHR J1709−3931	17:09:10.1	−39:31:06.50	347.030	+0.352	T		
PN H 1-7	17:10:27.4	−41:52:49.40	345.277	−1.249	T	180.98	0.75
RPZM 3	17:11:25.2	−39:29:51.68	347.305	+0.015	P	30.43	0.41
PM 1-131	17:12:22.0	−42:30:41.26	344.976	−1.907	T	3.61	0.02
MPA J1713−4015	17:13:10.8	−40:15:56.09	346.883	−0.710	T	9.55	0.08
Kn 102	17:14:25.0	−41:44:34.00	345.822	−1.765	L		
PHR J1714−4006	17:14:49.3	−40:06:08.96	347.199	−0.869	T	11.52	0.07
MPA J1715−4303	17:15:15.9	−43:03:53.78	344.838	−2.662	T	10.87	0.06
CBF-3	17:15:46.8	−42:24:06.12	345.434	−2.354	T	5.28	0.03
RPZM 8	17:15:51.6	−39:33:08.24	347.763	−0.711	T	9.35	0.09

the local ISM and therefore to the next generation of stars. Moreover, SNRs release large amounts of energy, generating shock waves that propagate in the immediate surroundings with evident effects (shaping of ISM, triggering star-formation, etc.).

The most complete catalogue of Galactic SNRs is provided by Green (2019) on the basis of observations performed over the whole electromagnetic spectrum. The large majority of the classified SNRs (∼95 per cent) is identified as radio source.

In the ASKAP SCORPIO region there are 14 SNRs reported in Green (2019) and two candidates from the literature (Whiteoak & Green 1996), whose classification as SNRs has been recently supported by Ingallinera et al. (2019). All of them are visually detected in the SCORPIO map, and their main characteristics are summarized in Table 4. In the ASKAP map we also detect a further three SNR candidates, proposed by Ingallinera et al. (2019), namely SCO J165948−420527, SCO J170029−421309, and SCO J170105−420531.

SNRs are studied across the whole electromagnetic spectrum, but non-thermal radio emission remains their main identifier. The morphology and the spectral variations in the radio band are closely related to the evolutionary phase and the interaction of the SNR with the surrounding material. The possibility to observe these sources with high sensitivity and angular resolution in the radio band allows us to identify new SNRs and to perform detailed morphological and spectral characterization of the known ones. Indeed, both the age and the environmental conditions can affect the emission processes in SNRs, and the study of a larger sample of objects is crucial to their wider understanding and classification.

Due to the availability of very short baselines, ASKAP allowed us to reach an LAS of ∼50 arcmin at 912 MHz. This value, coupled with the high resolution, permits us to investigate SNRs at different angular scales, providing sensitive and detailed maps of these extended and complex sources. In the ASKAP map at 912 MHz, we can study the morphological details of the 16 known SNRs detected in the SCORPIO field. A 2.3 × 1.3 deg^2 portion of the map, centred at l = 343.8° b = −0.2°, is shown in Fig. 11, where four published SNRs (Green 2019) are highlighted with white circles and the three SNR candidates (Ingallinera et al. 2019) with green circles.

We stress here that the ASKAP mapping capabilities, illustrated in Fig. 4 for the SNR G343.1−0.7, allow us to distinguish the unrelated, field sources from the remnant itself. This results in a significant improvement in the estimation of the flux density of these SNRs with respect to previous images of these sources. Moreover, a previously classified SNR might be reclassified as S or C if observed with a better sensitivity and higher resolution.

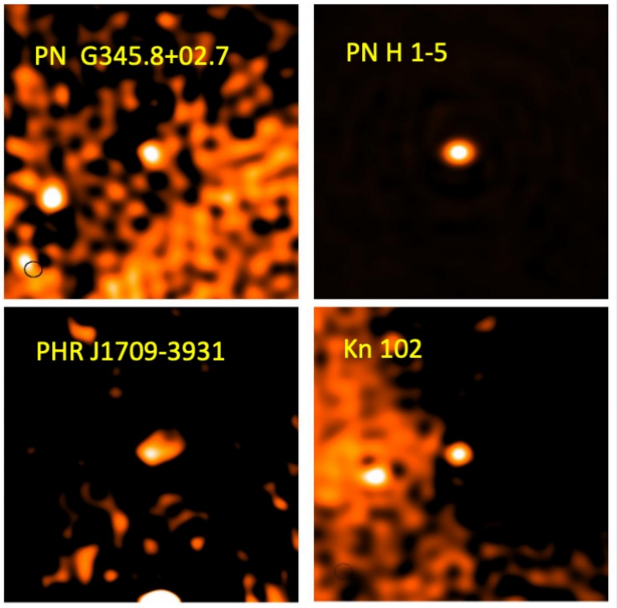

Figure 9. Maps of the detected PNe, including three new detections, which were not extracted by SELAVY, with no flux density indications in Table 3. All the images are 400 arcsec × 400 arcsec in size and centred at the PN's position (RA, Dec.).

In the radio, a large fraction of known SNRs present a typical 'shell-like' morphology, which is a strong indicator of their nature. There are many extended sources in the SCORPIO field that satisfy the morphological criterion for SNRs. Those sources constitute a very promising sample of SNR candidates. Observations at other frequencies, such as those already planned for the SCORPIO field between 0.9 and 1.8 GHz in the very near future, will be necessary to confirm the non-thermal origin of the radio emission.

4 THE SCORPIO PROJECT IN THE CONTEXT OF EMU: LESSONS LEARNT SO FAR

4.1 The impact of EMU on Galactic science

Radio surveys have provided a large number of unexpected discoveries, revealing different populations of radio-emitting objects and allowing numerous and very successful follow-up studies. An optimal radio survey of the Galactic plane needs to be carefully designed to correctly probe both the compact, extended and diffuse kinds of emission that populate the plane of the Galaxy. With previous and current radio facilities, this has been difficult to achieve in practice. The usual way to overcome this problem is the use of interferometric arrays in different antenna configurations and/or adding single-dish data. Up to now, existing interferometric radio continuum surveys of the Galactic plane cover a small portion of the Galactic plane (a few tens of square degrees), with high angular resolution (arcsecs) and sensitivity (1–2 mJy) (MAGPIS, Helfand et al. 2006; CORNISH, Hoare et al. 2012; THOR, Wang et al. 2018; GLOSTAR, Medina et al. 2019), or wider areas (several 100 square degrees) but with limited angular resolution (arcmins) and sensitivity (several mJy) (IGPS, Taylor et al. 2003, 2017; McClure-Griffiths et al. 2005; Stil et al. 2006).

There is therefore the necessity to have a well-designed survey of the Galactic plane, with a good compromise between sensitivity to extended diffuse emission and the ability to resolve more compact sources. This is particularly important for the Southern hemisphere, where the lack of such surveys has prevented us from gathering detailed information of the radio properties of different source populations in the third and fourth Galactic quadrants. EMU, with its high sensitivity and angular resolution coupled to excellent short-spacing *uv*-plane coverage that provides high sensitivity to extended structures, and the unique survey speed capability that characterizes ASKAP, will allow us to create the most sensitive wide-field atlas of Galactic continuum emission yet made in the Southern hemisphere.

We stress that while the analysis presented here refers to data obtained with a partial deployment of ASKAP antennas, the tremendous potential of ASKAP has been clearly evidenced. ASKAP will be a revolutionary instrument for radio astronomy and therefore the full potential of EMU for Galactic observations can be anticipated. From this preliminary analysis of SCORPIO data, we have already demonstrated the unique capability of ASKAP to map complex sources, such as those that populate the Galactic plane, at different angular scales and with high sensitivity.

The EMU survey of the Galactic plane will have a profound impact on our understanding of star formation and stellar evolution, on Galactic structure and the nature of diffuse emission, and will very likely find new classes of objects.

4.2 The role of SCORPIO in the EMU design study

Several pilot studies, closely matching EMU in sensitivity and resolution, have been carried out to guide the design, operation, and science of the EMU project, e.g. the ATLAS (Norris et al. 2006) and SCORPIO (Paper I) surveys. SCORPIO, covering an area of a few square degrees, is the only pilot study to focus on low Galactic latitude and is especially important for the characterization of the Galactic sub-mJy population, providing a solid base-level from which we can better design some aspects of EMU. Indeed most of the ASKAP data processing techniques were optimized for extragalactic fields, and a special effort needs to be made to adapt processing techniques to cope with the large-scale structure, and strong confusing sources encountered in the Galactic plane. Synthesis imaging in these areas of the sky is badly affected by the discrete and limited sampling of the *uv*-plane. In the image plane this unavoidable imperfection arising from a lack of information in the *uv*-plane translates first into imaging artefacts, which increase the background noise in a non-random manner. It also likely results in incorrect reconstruction of the brightness distribution of extended sources. These problems are indeed detected in the ASKAP maps, where extended sources and the Galactic diffuse emission are present.

However, the comparison with the MGPS and the ATCA observations of SCORPIO reveals that the artefacts are not more severe than what we might theoretically expect. Indeed, the comparison of the same fields as observed by MOST, ASKAP, and ATCA demostrates how ASKAP, even in this early-science phase, provides the best compromise between fine details and extended structures and shows a superior capability, compared to other radio facilities, to recover low-brightness diffuse emission up to angular scales comparable to its LAS, allowing us to efficiently probe different spatial scales in complex regions. This is particularly advantageous for Galactic studies.

A critical point in the ASKAP data reduction process is the gain calibration, performed as stated earlier by self-calibrating on bright sources automatically extracted from the observed field. The presence of diffuse emission and extended sources may result in poorly determined gain solutions. To overcome this limit, we constrained the self-calibration to regions of the *uv*-plane far from its

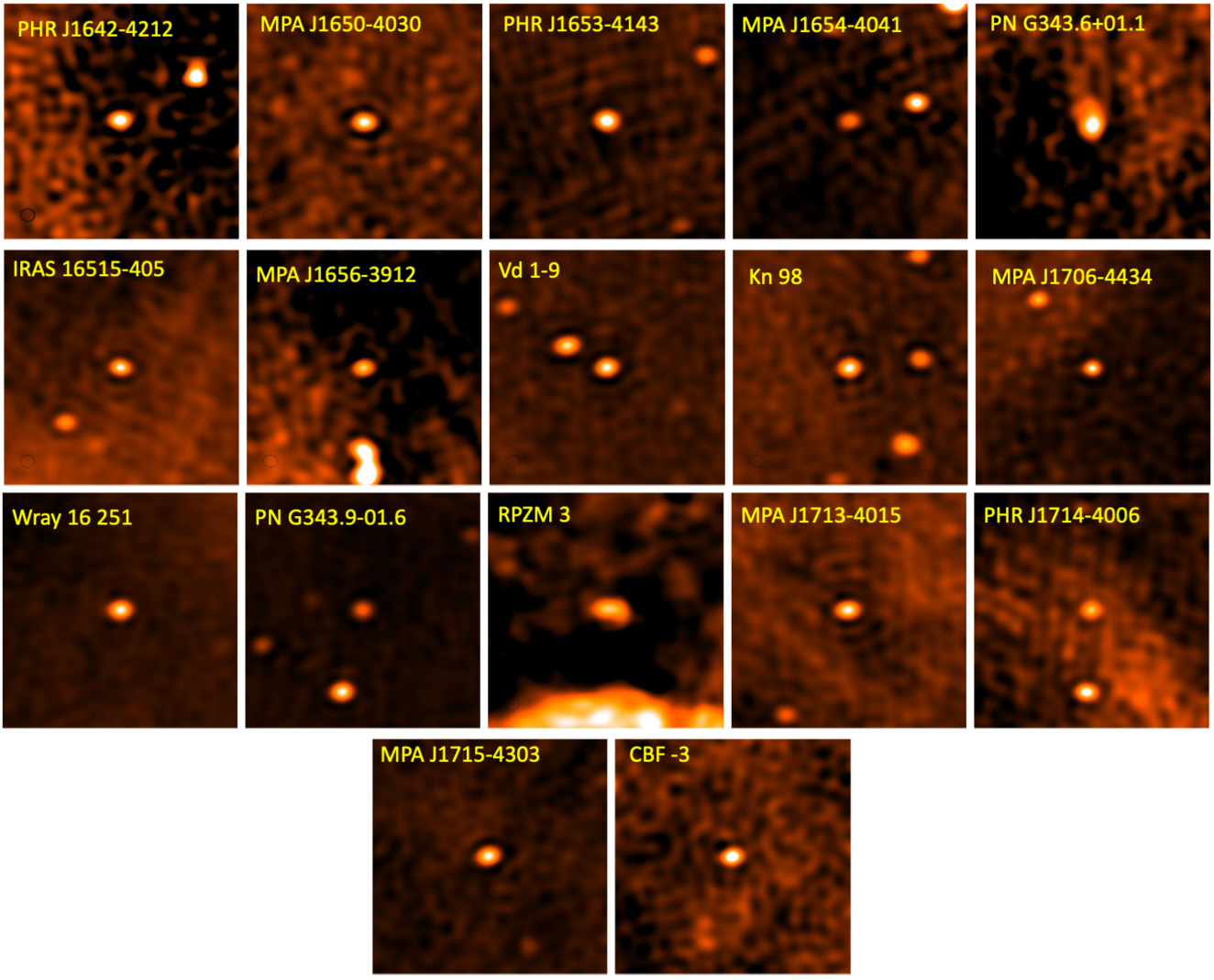

Figure 10. Maps of the new detected PNe, extracted by SELAVY (see Table 3). All the images are 400 arcsec × 400 arcsec in size and centred at the PN's position (RA, Dec.).

origin, i.e. restricting the analysis to long baselines (see Section 2.2). Several attempts were made in order to find an optimal setting that allowed us to filter out as much extended emission as possible but, at the same time, retain a sufficient number of baselines to derive reliable gain solutions. The ASKAP standard data reduction pipeline needs to be refined and adapted to this gain calibration process when applied to data acquired in the Galactic plane. A possible way to mitigate this problem is to design the EMU survey making sure to have a sequence of pointings, off the Galactic plane, alternating to pointings in the Galactic plane. This observing strategy would provide a sufficient number of point sources to be used for self-calibration.

The ASKAP observations were performed with three different pointings spaced by 51 arcmin, different from other fields observed with ASKAP in this early-science run. As reported in Section 2.2, two of these pointings, fields B and C, are corrupted by RFI. The automatic flagging algorithm embedded in the pipeline (CFLAG) failed to detect and flag these data. Another flagging utility (AOFLAGGER) was tested with similar results. Some single data sets have been visually inspected with CASA to check in detail whether the RFI were confined to particular time intervals or frequency ranges. Therefore, before merging the three fields, a manual flag for bad data improved imaging of fields B and C. However, this approach is not straightforward because of the large amount of data (around 9 TB per each field) and will become totally impractical with the full ASKAP array, and when observing larger sky areas. We suggest that the ASKAP standard data reduction pipeline should improve the automated algorithm to mitigate and flag the RFI, taking also into account possible effects that the applied flagging methods could have on extended bright sources as those populating the Galactic plane (Bihr et al. 2016).

An important part of all the pilot studies in the pre-SKA era is to acquire the experience in handling data from SKA precursors that are representative of SKA. A significant challenge with these huge data sets, beyond the data reduction itself, is to automatically find and classify radio sources. The size of SCORPIO field is still small enough to allow source identification by visual inspection, as done in this paper, but it is also sufficiently large for testing and training automated algorithms. Results from the human-driven visual inspection can be used as a verification check of the automated

Table 4. Summary of the known SNR detected with ASKAP at 912 MHz in the SCORPIO field, and related main characteristics. Type of the SNR: 'S' or 'C' if the remnant shows a 'shell' or 'composite' radio structure. We report the frequency range within which each source has already been observed. Source sizes are reported according to Green (2019).

Source name	Type	Frequency range (GHz)	Source size (arcmin^2)
G340.4−0.4*	S	0.330–5	10 × 7
G340.6+0.3	S	0.330–5	6 × 6
G341.2+0.9	C	0.330–1.425	22 × 16
G341.9−0.3	S	0.408–5	7 × 7
G342.0−0.2	S	0.408–5	12 × 9
G342.1+0.9	S	0.843–1.384	22 × 16
G343.1−0.7	S	0.843–8.55	27 × 21
G343.1−2.3	C?	0.330–8.46	32 × 32
G344.7−0.1	C?	0.408–11.2	8 × 8
G345.1−0.2	S?	0.843–1.4	6 × 6
G345.1+0.2	S	0.843	10 × 10
G345.7−0.2	S	0.843–5	6 × 6
G346.6−0.2	S	0.408–5	8 × 8
G347.3−0.5	S?	1.36	65 × 55
G348.5+0.1	S	0.08–14.7	15 × 15
G348.5−0.0*	S?	0.333–5	10 × 10

Note. *This SNR is only partially detected at the edge of our ASKAP map.

algorithms. The pilot survey of SCORPIO has been already used as a test-bed for automated tools to extract sources, such as the CAESAR algorithm (Riggi et al. 2016, 2019) that extracts and parametrizes sources from astronomical radio interferometric maps.

The task for identifying the most appropriate method of finding and extracting sources, embedded in the diffuse emission expected at low Galactic latitude, is still ongoing (Riggi et al. 2021). The performance of the most used source finding algorithms (SELAVY, CAESAR, and AEGEAN) has been tested and it is subject of an ongoing work (Riggi et al., in preparation). A major result is that the number of false detections, above a fixed detection threshold, is considerable regardless of the finder used. This is due to the overdeblending of real diffuse emission and extended sources in the Galactic plane and to the presence of artefacts, due to a non-perfect cleaning. Overall, this represents a severe issue for future, large-scale radio surveys covering the Galactic plane such as those planned with ASKAP.

It is clear that with the new generation of large-scale surveys, which will be produced by new instruments such as the SKA and its precursors, it will be necessary to develop new automated algorithms able not only to extract both extended and compact sources but also to classify them. In the context of Galactic studies, exploiting the possibility of comparing different morphologies or different properties that sources manifest at different wavelengths, in automated methods and using data mining capabilities, could be particularly useful.

4.3 Synergies with existing Galactic plane surveys

Our view of the plane of the Galaxy has been completely revolutionized by a new generation of Galactic plane surveys as summarized by Hoare et al. (2012). Of particular interest are the surveys conducted at infrared and longer wavelengths, which can penetrate the extinction in the Galactic plane, tracing stars and nebulae (VVV; Minniti et al. 2010; GLIMPSE, Churchwell et al. 2006), the cold (HiGAL; Molinari et al. 2010), the warm (MIPSGAL, Carey et al. 2009; WISE, Wright, Eisenhardt & Mainzer 2010), and hot dust (GLIMPSE). These new IR Galactic plane surveys are characterized by a few arcsecs angular resolution, matching the ASKAP angular resolution, and have a very good sensitivity and sky coverage, to allow IR and radio counterparts to be efficiently identified and studied. Studies of this kind will be facilitated by visual analytics tools that have been recently developed to assist scientists in managing, visualizing, and analysing large amount of data (Vitello et al. 2018).

While Galactic H II regions and PNe populations can be in principle discriminated by using IR colours derived by photometric measurements (Anderson et al. 2012) or studying their local environment (Irabor et al. 2018), in the case of H II regions and PNe, as well as for other classes of Galactic objects, robust classification can be achieved only by combining radio and IR information (Cohen et al. 2011).

The SCORPIO field, as observed by the ASKAP (see Fig. 2), reveals the striking 'bubbling' appearance of the Galactic plane, confirming what recent large-scale mid-IR surveys have revealed: the presence of hundreds of extended (scales from tens arcsec to arcminutes) gaseous and dusty nebulae ubiquitous in the Galactic plane. The term 'bubbles' is usually used to classify them, although they can be the result of different astrophysical phenomena: a bubble can be the result of the expansion of a young H II region into the ISM due to strong winds or radiation pressure from the central stellar object/s (Churchwell et al. 2006) or indicate the presence of circumstellar material, the signpost of instabilities that often characterize the late stages of stellar evolution (Gvaramadze, Kniazev & Fabrika 2010; Mizuno et al. 2010; Watcher et al. 2010). Such circumstellar envelopes (CSE) are often observed in PNe, LBVs, WRs, and SNRs. Several authors have pointed out that with enough resolution and sensitivity it is possible to classify Galactic bubbles, discriminating H II regions from evolved star CSEs, and among the latter low- and high-mass stars, just from the comparison of the observed morphology in the IR and in the radio (Watson et al. 2008; Deharveng et al. 2010; Ingallinera et al. 2016). Indeed, for H II regions or evolved stars, while the radio emission traces the ionized part of the circumstellar material, the emission observed in the IR traces emission from polycyclic aromatic hydrocarbons (PAH) and hot dust ($\sim$ 8 μm) or warm dust ($\sim$ 24 μm) or cool dust ($\sim$ 70 μm). In H II regions, the $\sim$ 8 μm emission is dominated by PAH, which cannot survive at the temperature of the inner region, where the radio emission originates. Therefore, a strong ($\sim$ 8 μm) emission 'wrapping around' the radio emission points towards an H II region classification (Deharveng et al. 2010; Ingallinera et al. 2019).

In the case of SNRs, there is evidence of dust signatures in several of them (Chawner et al. 2020). However, the ratio of mid-IR to radio continuum emission results to be much lower than the infrared to radio ratio observed in H II regions (Pinheiro Goncalves et al. 2011). This can be used as efficient diagnostics to discriminate between a thermal and a non-thermal emitting bubble. A similar anticorrelation between radio emission and 8 μm IR emission is also established (Brogan et al. 2006; Anderson et al. 2017).

There are many extended sources in the ASKAP SCORPIO field with a roundish or shell-like structure (bubbles) that satisfy the morphological criterion for SNRs but also for H II regions and evolved stars. Fig. 12 is a composite image of a portion of the ASKAP SCORPIO field, for $341^\circ \leq l \leq 348^\circ$ and $|b| \leq 1^\circ$ in both dust and ionized gas. Dust, as traced at 8 and 70 μm, and ionized gas, probed by the radio, are cospatial at large scales in star-forming regions associated with H II regions, while there is a clear lack of dust associated with the radio in the case of known SNRs. The extended sources detected in SCORPIO therefore constitute a very promising

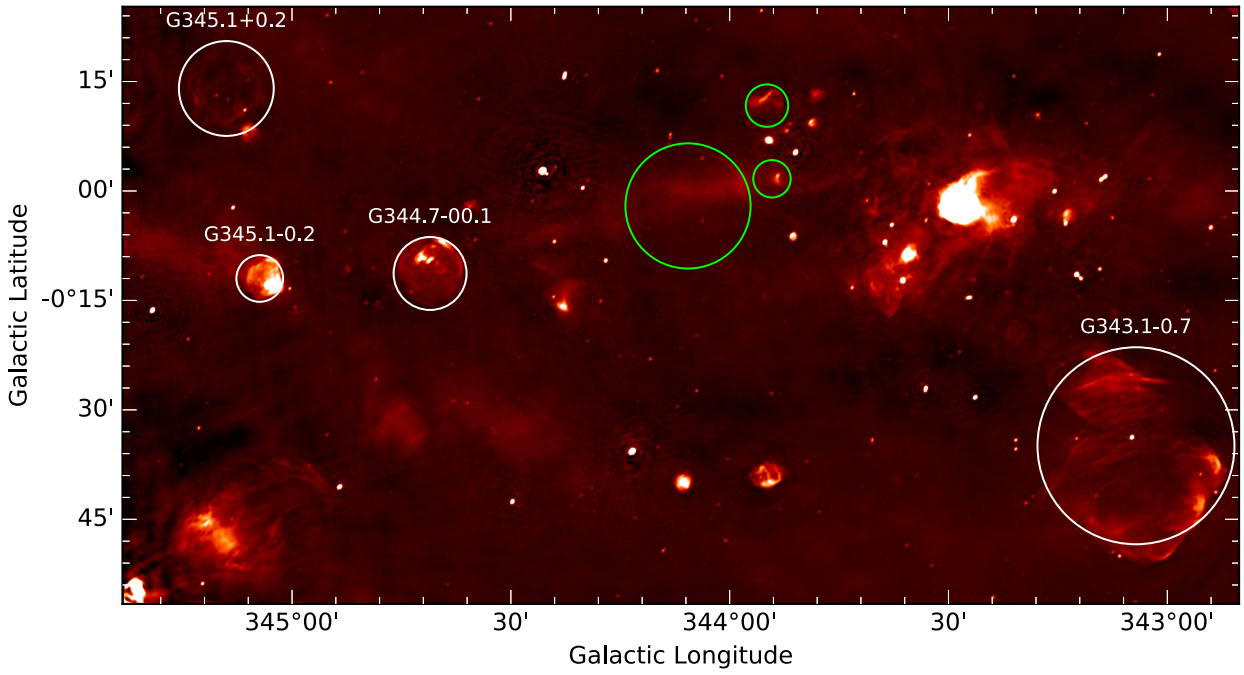

Figure 11. A zoom-in of the SCORPIO field, a 2.3 × 1.3 deg^2 portion of the map, centred at l,b = 343.8°, −0.2°. Known SNR (Green 2019) are highlighted with white circles, while proposed SNR candidates (Ingallinera et al. 2019) with green circles (see text for more details).

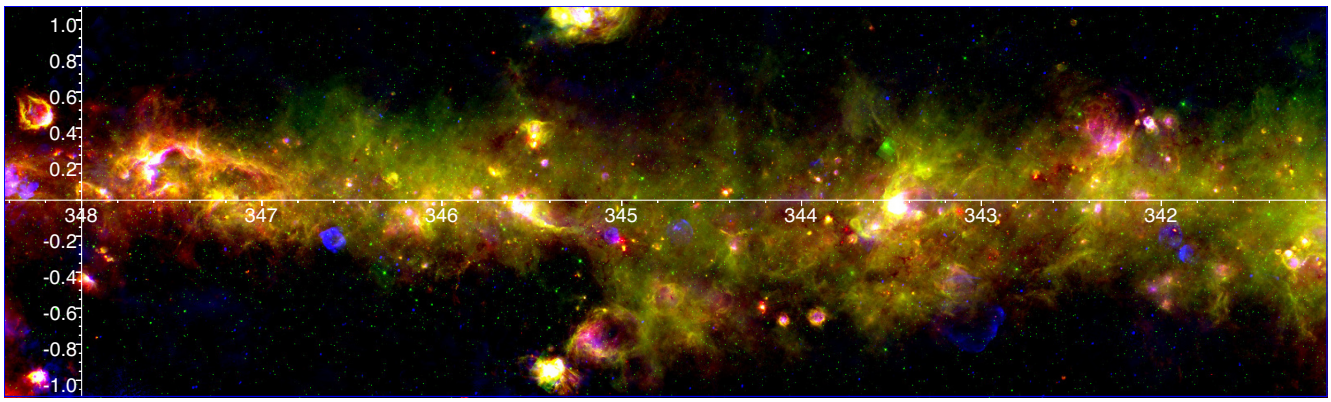

Figure 12. A composite image of a portion of the SCORPIO field (341° ≤ l ≤ 348°). The colour-code is: green, from Spitzer/Glimpse (IRAC, 8 μm); red, from Herschel/Hi-GAL (PACS, 70 μm) and blue from ASKAP, 912 MHz. The 8 and 70 μm emissions are tracers of the dust, while the radio emission traces of the ionized gas. Both dust and ionized emission are largely spatially coincident in star-forming regions, while there is very little correlation in the case of SNRs, which stand out due to their radio emission.

sample to classify the Galactic Bubbles and in particular to select new SNR candidates, by applying the criterion that bubbles with different origin are characterized by different IR emission, in both intensity and morphology. Different samples of 'bubbles' are in the process of being selected using these criteria. Further confirmation of their classification will be assessed on the basis of their radio spectra as determined by forthcoming planned ASKAP observations of the SCORPIO field at 0.9 and 1.8 GHz.

5 SUMMARY AND OUTLOOK

We present the ASKAP observations of the SCORPIO field, conducted in the ASKAP early-science framework. The ASKAP SCORPIO field was observed in band 1 (central frequency 912 MHz) with three different pointings, for a total area of ∼40 square degrees. The data were processed using the ASKAPSOFT data reduction pipeline (version 0.19). Some fine-tuning was needed with respect to the standard settings of the pipeline in order to better deal with data acquired towards the Galactic plane. In particular, the self-calibration process was limited only to regions of the *uv*-plane with $\sqrt{u^2+v^2} > 1100$ m. The final map presents a median rms of 541 μJy beam^{-1}, but as low as 130 μJy beam^{-1} in regions far from the Galactic plane.

A total of 3545 sources were extracted from the image, only 75 per cent of them are compatible with a point source. The presence

of a significant number of extended sources can be accounted for by Galactic sources, mainly H II regions. The comparison with the same areas of the Galactic plane as observed with the MGPS survey demonstrates the unique ASKAP capability of mapping complex sources, at different angular scales, with a trade-off between sensitivity to extended and diffuse emission and ability to reveal the finest details. This is the result of the ASKAP design to image wide fields with particular attention to the *uv*-coverage from short-baselines.

The SCORPIO project has been designed to forecast the scientific impact of the SKA and its precursors, such as ASKAP, on our view of the Milky Way. At the same time, SCORPIO has been considered as a test-bed to identify, and possibly overcome, technical issues arising from the complex structure of the Galactic plane. It is clear that SCORPIO has accomplished both its scientific and technical tasks. In particular, a good estimation of the potential of deep radio surveys for Galactic studies has been established.

Even with the presented results, obtained with ASKAP not fully deployed, the detection fraction of different Galactic populations emitting in the radio band has been significantly improved. We were able to detect all the known radio-emitting H II regions contained in the ASKAP SCORPIO field, and also a significant portion of H II regions previously classified as 'radio quiet'. We have doubled the number of radio detections for PNe within the ASKAP SCORPIO field and obtained a detailed morphology of known and candidate SNRs. Our results have been achieved by visual inspection at positions from relevant, mostly optical, catalogues. When complete radio multifrequency and polarization information, obtained with the full array, is available, as planned in the near future for SCORPIO and more in general with EMU, it will be possible to identify different Galactic source populations, disentangling thermal and non-thermal emitters or pick-up stellar radio sources just from their polarization characteristics (Dulk & Marsh 1982). With regards to SNRs, SCORPIO ASKAP observations have already highlighted the effectiveness in searching for new candidates.

We plan to focus our future activities on discovering and characterizing different populations of Galactic sources and to work at least on the following topics: (a) complete catalogue of extended sources, including H II regions, SNRs, and more evolved PNe; (b) Characterization of known SNRs and classification of SNR candidates via multiband radio observations in synergy with mid-IR observations; and (c) Multiwavelength study of the SCORPIO field in synergy with mid-IR observations aimed at identifying new H II region, SNR, LBV, WR, and PN candidates and revealing the complete picture of complex regions within the field (i.e. giant molecular clouds).

ACKNOWLEDGEMENTS

The Australian SKA Pathfinder is part of the Australia Telescope National Facility which is managed by CSIRO. Operation of ASKAP is funded by the Australian Government with support from the National Collaborative Research Infrastructure Strategy. Establishment of the Murchison Radio-astronomy Observatory was funded by the Australian Government and the Government of Western Australia. This work was supported by resources provided by the Pawsey Supercomputing Centre with funding from the Australian Government and the Government of Western Australia. We acknowledge the Wajarri Yamatji people as the traditional owners of the Observatory site. HA has benefitted from grant CIIC 90/2020 of Universidad de Guanajuato, Mexico. MJM acknowledges the support of the National Science Centre, Poland through the SONATA BIS grant 2018/30/E/ST9/00208. C. B. benefited from grant No. 863448 (NEANIAS) of the Horizon 2020 European Commission programme. This research has made use of the HASH PN database at hashpn.space.

DATA AVAILABILITY

The data underlying this article will be shared on reasonable request to the corresponding author.

REFERENCES

Anderson L. D., Bania T. M., Blaser D. S., Cunningham V., Wenger T. V., Johnstone B. M., Armentrout W. P., 2014, ApJS, 212, 1
Anderson L. D., Zavagno A., Barlow M. J., García-Lario P., Noriega-Crespo A., 2012, A&A, 537, 1A.
Anderson L. D. et al., 2017, A&A, 605, A58
Armentrout W. P., Anderson L. D., Wenger T. V., Balser D. S., Bania T. M, 2021, ApJS, 253, 23A
Becker R. H., White R. L., Helfand D. J., 1995, ApJ, 450, 559
Bihr S. et al., 2016, A&A, 586, A97
Brogan C. L., Gelfand J. D., Gaensler B. M., Kassim N. E., Lazio T. J. W., 2006, ApJ, 639, L25
Carey S. J. et al., 2009, PASP, 121, 76
Cavallaro F. et al., 2018, MNRAS, 473, 1685
Chawner H. et al., 2020, MNRAS, 493, 2706
Chippendale A. P., Hayman D., Hay S. G., 2014, Publ. Astron. Soc. Aust., 31, 19
Churchwell E. et al., 2006, ApJ, 649, 759
Cohen M. et al., 2011, MNRAS, 413, 542
Condon J. J., Kaplan D. L., 1998, ApJS, 117, 361
Deharveng L. et al., 2010, A&A, 523, A6
Dulk G. A., Marsh K. A., 1982, ApJ, 259, 350
Egron E. et al., 2017, MNRAS, 470, 2
Green D. A., 2019, JA&A, 40, 36
Gvaramadze V. V., Kniazev A. Y., Fabrika S., 2010, MNRAS, 405, 1047
Helfand D. J., Becker R. H., White R. L., Fallon A., Tuttle S., 2006, AJ, 131, 2525
Hoare M. et al., 2012, PASP, 124, 939
Hotan A. W. et al., 2021, Publ. Astron. Soc. Aust., 38, 9
Ingallinera A. et al., 2016, MNRAS, 463, 723
Ingallinera A. et al., 2019, MNRAS, 490, 5063
Irabor T. et al., 2018, MNRAS, 480, 2423
Jacoby G. H. et al., 2010, Publ. Astron. Soc. Aust., 27, 156
Kwok S., 2007, The Origin, Evolution of Planetary Nebulae. Cambridge University Press, Cambridge, UK
Leahy D. A. et al., 2019, Publ. Astron. Soc. Aust., 36, 24L
McClure-Griffiths N. M. et al., 2005, ApJS, 158, 178
McConnell D. et al., 2016, Publ. Astron. Soc. Aust., 33, e042
Medina S.-N. X. et al., 2019, A&A, 627, 175
Minniti D. et al., 2010, New Astron., 15, 433
Mizuno D. R. et al., 2010, AJ, 139, 1542
Molinari S. et al., 2010, A&A, 518, L100
Murphy T., Mauch T., Green A., Hunstead R. W., Piestrzynska B., Kels A. P., Sztajer P., 2007, MNRAS, 382, 382
Norris R. P. et al., 2006, AJ, 132, 2409
Norris R. P. et al., 2011, Publ. Astron. Soc. Aust., 28, 215
Parker Q. A., Bojičić I. S., Frew D. J., 2016, J. Phys. Conf. Ser., 728, 032008
Pinheiro Goncalves D. et al., 2011, AJ, 142, 47
Riggi S. et al., 2016, MNRAS, 460, 1486
Riggi S. et al., 2019, Publ. Astron. Soc. Aust., 36, 37
Riggi S. et al., 2021, MNRAS, 502, 60
Sabin L. et al., 2014, MNRAS, 443, 3388
Stil J. M. et al., 2006, AJ, 132, 1158
Tammann G. A., Loeffler W., Schroeder A., 1994, ApJS, 92, 487.
Taylor A. R., et al, 2003, AJ, 125, 3145
Taylor A. R. et al., 2017, AJ, 153, 113

Umana G. et al., 2015, MNRAS, 454, 902
Vitello et al., 2018, Publ. Astron. Soc. Aust., 130, 084503
Wang Y. et al., 2018, A&A, 619, A124
Watcher S. et al., 2010, AJ, 139, 2330
Watson C. et al., 2008, ApJ, 681, 1341
Whiteoak J. B. Z., Green A. J., 1996, A&AS, 118, 329
Whiting M.software ASKAP Science Data Processor, et al., software ASKAP Science Data Processor 2019, Available at: https:// bitbucket.csiro.au/scm /casssoft/askapsoft.git
Whiting M., Humphrey B., 2012, Publ. Astron. Soc. Aust., 29, 371
Wright E. L., Eisenhardt P. R. M., Mainzer A. K., 2010, AJ, 140, 1868

SUPPORTING INFORMATION

Supplementary data are available at *MNRAS* online.

Table S1. H II regions and H II regions candidates detected and extracted with SELAVY. This truncated table is intended to show its content. The complete table is available in the online version of the journal.

Please note: Oxford University Press is not responsible for the content or functionality of any supporting materials supplied by the authors. Any queries (other than missing material) should be directed to the corresponding author for the article.

This paper has been typeset from a TEX/LATEX file prepared by the author.